The Astrophysical Journal, 697:758–768, 2009 May 20 doi:10.1088/0004-637X/697/1/758
© 2009. The American Astronomical Society. All rights reserved. Printed in the U.S.A.

CORRELATED OPTICAL AND X-RAY FLARES IN THE AFTERGLOW OF XRF 071031

T. Krühler[1,2], J. Greiner[1], S. McBreen[1,3], S. Klose[4], A. Rossi[4], P. Afonso[1], C. Clemens[1], R. Filgas[1], A. Küpcü Yoldaş[5], G. P. Szokoly[6], and A. Yoldaş[1]

[1] Max-Planck-Institut für extraterrestrische Physik, Giessenbachstraße, 85748 Garching, Germany; kruehler@mpe.mpg.de
[2] Universe Cluster, Technische Universität München, Boltzmannstraße 2, 85748, Garching, Germany
[3] School of Physics, University College Dublin, Dublin 4, Republic of Ireland
[4] Thüringer Landessternwarte Tautenburg, Sternwarte 5, 07778 Tautenburg, Germany
[5] European Southern Observatory, Karl-Schwarzschild-Straße 2, 85748 Garching, Germany
[6] Institute of Physics, Eötvös University, Pázmány P. s. 1/A, 1117 Budapest, Hungary
Received 2008 December 23; accepted 2009 March 3; published 2009 May 5

ABSTRACT

We present a densely sampled early light curve of the optical/near-infrared (NIR) afterglow of the X-Ray Flash (XRF) 071031 at $z = 2.692$. Simultaneous and continuous observations in seven photometric bands from g' to K_S with GROND (Gamma-Ray Burst Optical/Near-InfraRed Detector) at the 2.2-m MPI/ESO telescope on LaSilla were performed between 4 minutes and 7 hr after the burst. The light curve consists of 547 individual points which allows us to study the early evolution of the optical transient associated with XRF 071031 in great detail. The optical/NIR light curve is dominated by an early increase in brightness which can be attributed to the apparent onset of the forward shock emission. There are several bumps which are superimposed onto the overall rise and decay. Significant flaring is also visible in the *Swift* X-Ray Telescope (XRT) light curve from early to late times. The availability of high-quality, broadband data enables detailed studies of the connection between the X-ray and optical/NIR afterglow and its color evolution during the first night postburst. We find evidence of spectral hardening in the optical bands contemporaneous with the emergence of the bumps from an underlying afterglow component. The bumps in the optical/NIR light curve can be associated with flares in the X-ray regime suggesting late central engine activity as the common origin.

Key words: gamma rays: bursts – X-rays: individual (XRF 071031)

Online-only material: color figure

1. INTRODUCTION

Major progress in the understanding of the X-ray and optical afterglow light curves of gamma-ray bursts (GRBs) and the softer X-Ray Flashes (XRFs) has been made since the launch of the *Swift* satellite (Gehrels et al. 2004) and the rapid follow-up data provided by the X-Ray Telescope (XRT; Burrows et al. 2005b) and Ultra-Violet Optical Telescope (UVOT; Roming et al. 2005). However, access to the longer wavelength afterglow is still somewhat limited to the brighter half of all detected bursts. In contrast to the evidence of a generic X-ray afterglow light curve (Nousek et al. 2006), the few bursts with very early detected optical counterparts show a considerable variety. For instance, GRBs 990123 (Akerlof et al. 1999) and 041219A (Blake et al. 2005; Vestrand et al. 2005; McBreen et al. 2006) have shown optical emission contemporaneous with the prompt phase of the burst. A significant delay in the apparent onset of the afterglow forward shock (FS) allowed ground-based optical/near-infrared (NIR) telescopes to detect a rising component of the afterglows for, e.g., GRBs 030418 (Rykoff et al. 2004), 060418, 060607A (Molinari et al. 2007), 070802 (Krühler et al. 2008), and 071010A (Covino et al. 2008). A number of optical afterglows showed bumps superimposed onto the overall power-law decay in late epochs which are generally interpreted as the signature of either inhomogeneities in the circumburst medium (e.g., GRB 050502A; Guidorzi et al. 2005) or late energy injections (e.g., GRB 021004, de Ugarte Postigo et al. 2005 or GRB 070311, Guidorzi et al. 2007).

The very early optical afterglow is of significant interest from a theoretical point of view and in particular how it relates to the flares and plateaus seen in many X-ray afterglow light curves (e.g., O'Brien et al. 2006). In the early phase, the color evolution is crucial to differentiate between different emission components. However, most of the rapid ground-based follow-up is obtained with robotic telescopes of small aperture size in white light or filter cycles. In both cases, information about the spectral properties is absent or can only be obtained at relatively long times with respect to the dynamical timescale in the early evolution of GRB emission. The ambiguity between effects of a changing spectrum or a highly variable early light curve can only be addressed by systematic observations in different broadband filters as synchronous and rapid as possible. Comprehensive data sets of early optical afterglows were published, e.g., for GRB 021004 (Lazzati et al. 2002), GRB 030329 (Lipkin et al. 2004), GRB 061126 (Perley et al. 2008), and the very bright GRB 080319B (e.g., Racusin et al. 2008) where the light curve is well sampled in time and frequency domains, suggesting that a standard jet break model alone cannot account for the increasing variety of features in a GRB or XRF afterglow.

Here, we report on the optical follow-up of GRB 071031 at redshift 2.692 (Ledoux et al. 2007) using data obtained in seven broadband filters from g' to K_S with the multichannel imager GROND (Greiner et al. 2007, 2008). Ground-based optical/NIR observations started at ∼4 minutes after trigger, yielding one of the best sampled early optical light curves. In combination with the detailed X-ray observations provided by the XRT, this constitutes a multicolor light curve with spectral coverage from the NIR to the 10 keV XRT band.

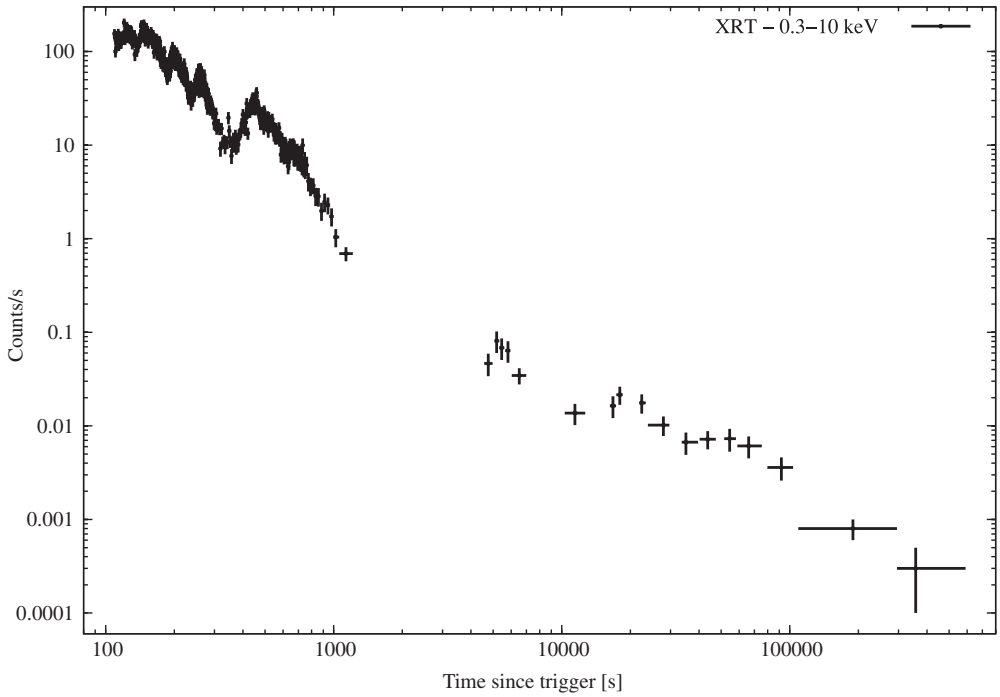

Figure 1. *Swift* XRT light curve of the X-ray afterglow of XRF 071031 obtained from the XRT light curve repository (Evans et al. 2007).

2. OBSERVATIONS

2.1. *Swift*

The Burst Alert Telescope (BAT; Barthelmy et al. 2005) onboard the *Swift* satellite triggered on the long-soft GRB 071031 at T_0 = 01:06:36 UTC and immediately slewed to the burst (Stroh et al. 2007b). The BAT light curve shows a two-peaked structure starting at $T_0 - 10$ s and ending at T_0+180 s with a T_{90} of 180 ± 10 s. The fluence in the 15 to 150 keV band is $9.0 \pm 1.3 \times 10^{-7}$ erg cm^{-2}, with a fluence ratio of 1.34 between the BAT 25–50 and 50–100 keV bands (Stamatikos et al. 2007). This is remarkably soft compared to conventional GRBs and qualifies GRB 071031 as an XRF according to the working definition of Sakamoto et al. (2008). The BAT spectrum of the first peak is well described with a single power law with a photon index of 2.26 ± 0.30 ($\chi^2 = 28.83$ for 36 degrees of freedom (dof)). This is well outside the normal range for the low energy index α but similar to the spectral index β above the break energy for a Band function (Band et al. 1993; Preece et al. 2000). The peak energy of the prompt emission spectrum must then be close to or below the BAT lower energy range of around 30 keV (see also McGlynn et al. 2005; Stamatikos et al. 2007). Therefore, GRB 071031 is designated as XRF 071031 hereafter.

The XRT began follow-up observations of the burst field 103 s after the trigger and detected an uncataloged fading X-ray source at a position of R.A.(J2000) = $00^h\,25^m\,37\overset{s}{.}4$, decl.(J2000) = $-58^\circ\,03'\,33''$ with a refined 90% confidence error circle of $2\overset{''}{.}0$ radius (Stroh et al. 2007a). The early XRT light curve is dominated by a significant amount of flaring with bright flares at around 120, 150, 200, 250, and 450 s. Also the late X-ray data exhibit rebrightenings at 5.5, 20, and 55 ks superimposed onto the overall power-law decay. The complete XRT light curve is shown in Figure 1.

The X-ray spectra were obtained with the `xrtpipeline` tool using the latest calibration frames from the *Swift* CALDB and standard parameters. The spectra were fitted with the XSPEC package (Arnaud 1996) and a foreground hydrogen column density at the Galactic value of $N_{\rm H} = 1.2 \times 10^{20}$ cm^{-2} (Kalberla et al. 2005).

The third instrument onboard *Swift*, UVOT started observations at T_0+114 s and found a transient source inside the XRT error circle in the white, *v*- and *b*-band filters. The UVOT data show an increase in the brightness of the afterglow of around 0.5 mag in the first few hundred seconds (Breeveld & Stroh 2007).

2.2. *GROND*

GROND responded to the *Swift* GRB alert and initiated automated observations that started at 01:10:21 UTC, 3 minutes 45 s after the burst and continued until local Sunrise at 08:55:51 UTC. A predefined sequence of observations with successively increasing exposure times was executed and images were acquired in all seven photometric bands simultaneously. In total 84 individual frames in each $g'r'i'z'$ and 1510 images of 10 s exposures in JHK_S were obtained during the first night at airmasses between 1.1 and 2.4. The integration time of the CCD optical images scaled from 45 to 360 s according to the brightness of the optical afterglow. A variable point source was detected in all bands (Krühler et al. 2007) by the automated GROND pipeline (Küpcü-Yoldaş et al. 2008), and its absolute position is measured to R.A.(J2000) = $00^h\,25^m\,37\overset{s}{.}24$, decl.(J2000) = $-58^\circ\,03'\,33\overset{''}{.}6$ compared to USNO-B reference field stars (Monet et al. 2003) with an astrometric uncertainty of $0\overset{''}{.}3$. Photometry and spectroscopy of the afterglow were also obtained by telescopes at Cerro Tololo Inter-American Observatory (CTIO) (Haislip et al. 2007; Cobb 2007) and the VLT, the latter yielding a UVES and FORS spectroscopic redshift of 2.692 (Ledoux et al. 2007; Fox et al. 2008).

Photometric calibration was performed relative to the magnitudes of 10 secondary standards in the field of XRF 071031, shown in Figure 2 and Table 1. During photometric conditions, three spectrophotometric standard stars, SA114-750, SA114-656, and SA95-42, all primary Sloan standards (Smith et al.

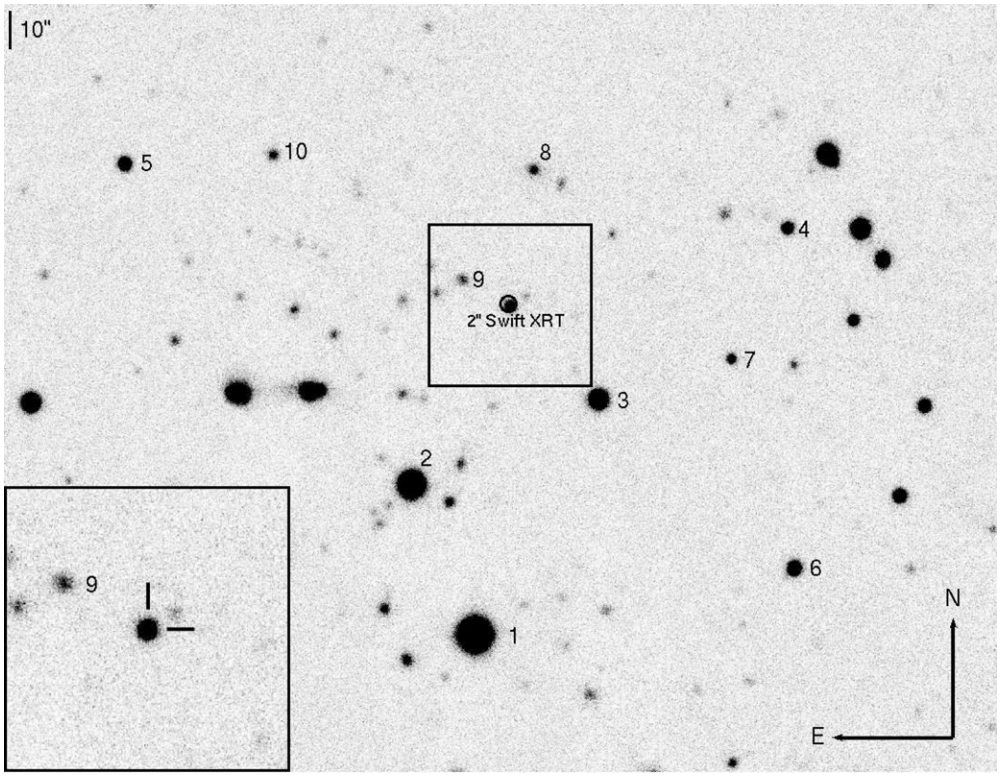

Figure 2. GROND r'-band image showing the afterglow of XRF 071031 and the XRT error circle. The secondary standards used for calibration are labeled 1 to 10 and listed in Table 1. The lower left corner shows a zoom in to the afterglow position.

2002), were observed with GROND. Observations of the GRB field followed within a few minutes. The magnitudes of the Sloan standards were transformed to the GROND filter system using their spectra and the GROND filter curves (Greiner et al. 2008). The obtained zeropoints were corrected for atmospheric extinction differences and used to calibrate the stars in the GRB field. An independent absolute calibration was obtained with respect to magnitudes of the Sloan Digital Sky Survey (SDSS) and Two Micron All Sky Survey (2MASS) stars within the standard fields obtained from the SDSS data release 6 (Adelman-McCarthy et al. 2008) and the 2MASS catalog (Skrutskie et al. 2006) with results consistent with the standard star calibration at the 0.03 mag level.

Optical and NIR image reduction and photometry were performed using standard IRAF tasks (Tody 1993). For each frame a model of the point spread function (PSF) was constructed using brighter field stars, and fitted to the afterglow. The relatively large seeing between 2″ and 3″ together with the pixel scale of 0.″16 for $g'r'i'z'$ and 0.″60 for JHK_S resulted in an excellent spatial sampling of the PSF with statistical fit errors of the order of 0.2% for $g'r'i'z'$ and 0.5% for JHK_S. For consistency, we also performed standard aperture photometry with compatible results with respect to the reported PSF photometry. All data were corrected for a Galactic foreground reddening of $E_{B-V} = 0.012$ mag in the direction of the burst (Schlegel et al. 1998).

The stacking of individual images was done twice for different purposes. First, all available data were used and individual frames were stacked until a statistical error in the PSF fit of around 0.1 mag was obtained. This resulted in 75 frames in each $g'r'i'$, 51 in z', 118 in J, and 76 in each H and K_S, yielding the multiwavelength light curve shown in Figure 3. Second, only NIR data simultaneous to the optical integrations were selected, excluding the frames which were taken during the $g'r'i'z'$ CCD

Table 1
Secondary Standards in the GRB Field in the GROND Filter Bands from 1 to 10

R.A./Decl. (Deg [J2000])	g' (mag)	r' (mag)	i' (mag)	z' (mag)	J (mag)	H (mag)	K_S (mag)
6.4098/−58.0831	15.44 ± 0.02	14.55 ± 0.02	14.28 ± 0.02	14.13 ± 0.02	13.09 ± 0.04	12.55 ± 0.04	12.50 ± 0.06
6.4186/−58.0723	16.32 ± 0.02	15.73 ± 0.02	15.54 ± 0.02	15.43 ± 0.02	14.46 ± 0.04	14.07 ± 0.04	14.00 ± 0.06
6.3933/−58.0662	17.84 ± 0.03	17.32 ± 0.03	17.18 ± 0.03	17.10 ± 0.03	16.18 ± 0.04	15.94 ± 0.06	15.65 ± 0.07
6.3672/−58.0536	20.71 ± 0.05	19.33 ± 0.03	18.53 ± 0.03	18.13 ± 0.03	16.86 ± 0.05	16.41 ± 0.07	16.28 ± 0.08
6.4579/−58.0492	20.03 ± 0.04	18.90 ± 0.03	18.49 ± 0.03	18.31 ± 0.03	17.07 ± 0.05	16.68 ± 0.07	16.45 ± 0.08
6.3663/−58.0782	20.09 ± 0.04	18.62 ± 0.03	17.60 ± 0.03	17.13 ± 0.03	15.80 ± 0.04	15.30 ± 0.05	14.92 ± 0.06
6.3751/−58.0631	21.26 ± 0.05	20.13 ± 0.04	19.72 ± 0.04	19.52 ± 0.04	18.29 ± 0.07	17.87 ± 0.08	17.79 ± 0.10
6.4021/−58.0496	22.72 ± 0.10	20.85 ± 0.05	20.06 ± 0.05	19.65 ± 0.05	17.94 ± 0.06	17.35 ± 0.07	16.11 ± 0.08
6.4117/−58.0575	22.49 ± 0.08	21.21 ± 0.06	20.76 ± 0.06	20.51 ± 0.07	18.56 ± 0.07	17.78 ± 0.08	16.86 ± 0.10
6.4375/−58.0485	21.28 ± 0.05	20.77 ± 0.05	20.61 ± 0.05	20.59 ± 0.07	19.29 ± 0.09	18.91 ± 0.10	17.98 ± 0.15

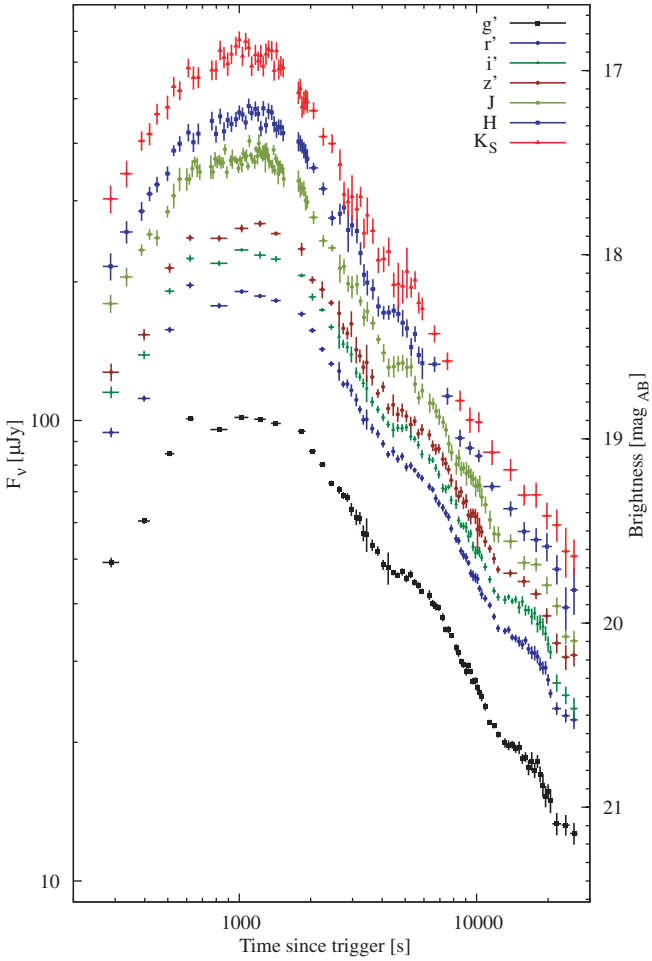

Figure 3. GROND optical and NIR light curve of the afterglow of XRF 071031 taken between ∼4 minutes and 7 hr after the trigger.

(A color version of this figure is available in the online journal.)

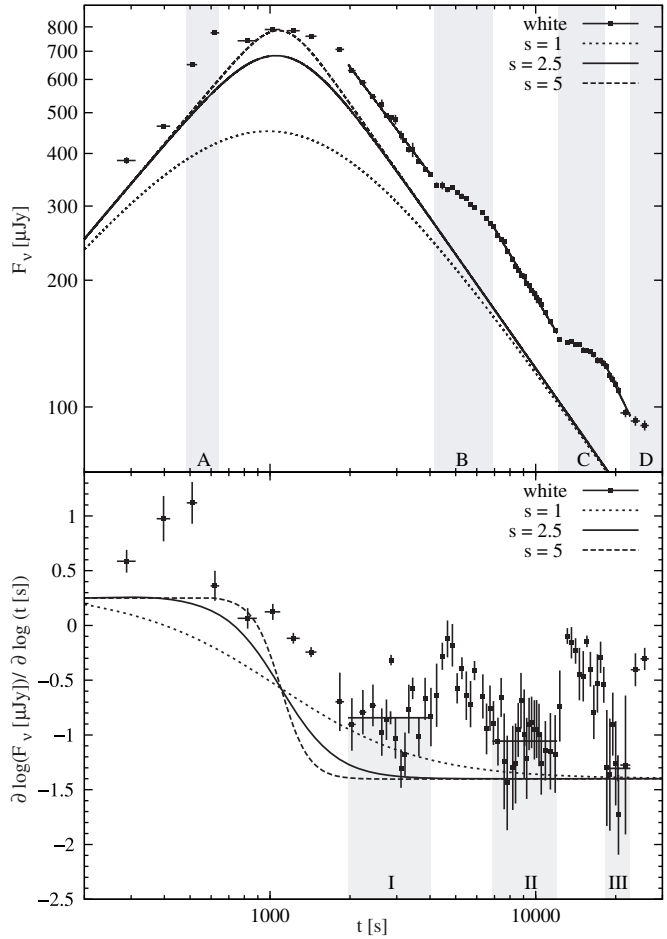

Figure 4. White light curve of the afterglow of XRF 071031 in the upper panel. A numerical differentiation of the data in the native log–log scale is shown in the lower panel. Regions of bumpiness are denoted with capital letters (upper panel) and the steeping of the power law in roman numbers (lower panel). The effect of a changing smoothness parameter s of the turnover is indicated by different lines in both panels.

read out. The resulting NIR image stacks were used to derive the optical to NIR spectral energy distribution (SED).

3. ANALYSIS

3.1. The Optical/NIR Light Curve

The multicolor light curve of XRF 071031 is complex and not described by smoothly connected power laws alone (Figure 3). Evident in all colors is the initial increase in brightness up to ∼1 ks, which smoothly turns over to a generic power-law decline with superimposed variations. In order to study small-scale irregularities at the highest possible signal-to-noise, a white light curve was derived by combining all $g'r'i'z'$ CCD data (Figure 4, upper panel), which are exactly synchronous by hardware setup. The NIR bands are excluded from this process due to the intrinsically larger photometric error which would serve only to increase the uncertainties in the summed data.

In order to better visualize the afterglow light curve, it is also presented differentiated in its native log–log scale, i.e. $\delta(\log(F_\nu))/\delta(\log(t))$, which directly represents the local power-law decay index $\alpha(t)$ (Figure 4, lower panel). On a log–log scale, the first derivative of a power law is a constant, so for a smoothly connected power-law rise and decay, one would expect a positive constant at early, turning into a negative at later times. Changes in the power-law index and deviations from the decay are clearly visible in this representation.

Without imposing an a priori model of the afterglow, Figure 4 convincingly demonstrates that the overall trend of the light curve is well described by two smoothly connected power laws as introduced in Beuermann et al. (1999). In both panels of Figure 4, however, the deviations from a Beuermann-like power-law rise and decay are clearly apparent. There are two features which require either a superimposed component or a different parameterization of the intrinsic afterglow. The first and most obvious is the additional emission component in regions A,B,C,D shown in the upper panel of Figure 4. This extra emission requires features intrinsic to the source or its environment to produce the observed flux excess with respect to the power law. The second is the steepening of the power-law decline after a rebrightening from region I over II to III in the lower panel of Figure 4. However, there is so much variability within the light curve that the underlying afterglow cannot be established with high certainty.

The early rising component in the optical bands might be related to the deceleration of the FS by the circumburst medium, which happens when the swept up medium efficiently decelerate the ejecta. From the time of the light curve peak, the initial bulk Lorentz factor of the outflow Γ_0 can be constrained. Using the formalism outlined by Sari & Piran (1999), Panaitescu & Kumar (2000), and Molinari et al. (2007), Γ_0 is estimated

to $\approx 90(\frac{E_{53}}{\eta_{0.2}A^*})^{1/4}$ in a wind shaped circumburst medium and to $\approx 200(\frac{E_{53}}{\eta_{0.2}n})^{1/8}$ for an interstellar medium (ISM)-type environment, with a weak dependence on the uncertain parameters A^* being the normalized wind density, E_{53} the isotropic-equivalent energy released in γ-rays in 10^{53} erg, $\eta_{0.2}$ the radiative transfer efficiency normalized to 0.2 and n the ISM density in cm^{-3}. The slow rise with a power-law index of $\sim$0.7 suggests a windlike environment, which would only be consistent with the closure relations for a very hard electron index (Dai & Cheng 2001) of $p \sim 1.6$ and $\nu_c < \nu$ using the spectral and temporal slopes in the late afterglow light curve $\alpha_{X,o} \sim 1$ and $\beta_X = 0.8 \pm 0.1$. The classical closure relations (e.g., Zhang & Mészáros 2004), however, would favor an ISM environment in the slow cooling case with $\nu_m < \nu < \nu_c$ and a more canonical value of $p \sim 2.6$.

Alternatively, the initial rise could be the result of a structured outflow seen off-axis (e.g., Panaitescu et al. 1998). In the case of previous fast and slowly rising afterglow light curves, Panaitescu & Vestrand (2008) find an anticorrelation of peak flux in the R band $F_{\nu,R}$ and peak time t_p. K-correcting the afterglow to $z = 2$ to match the previous sample, we find that the optical/NIR light curve of XRF 071031 fits very well into this anticorrelation. In this interpretation, the slow rise would hint on a large offset of the observer relative to the jet's symmetry axis.

Chromaticity around peak brightness was tested by comparing the optical/NIR SED before and after the total maximum. Apart from changes in the spectral index which can be attributed to the emergence of the bumps (see Section 3.4 and Figure 7), there is no evidence for a change in the spectrum before and after the light curve peak. The time of the light curve maximum is not correlated with energy, and all bands peak at a similar time within the measurement uncertainties. Such evolution would be expected if the main peak was caused by cooling of the ejecta after the prompt emission resulting in the shift of the characteristic synchrotron frequency ν_m into the optical bands (e.g., Ziaeepour et al. 2008). In addition, a moving ν_m through the optical bands is expected to cause a strong change from a positive to negative spectral index (e.g., Sari et al. 1998; Granot & Sari 2002). Neither effect is observed.

After correcting for Galactic foreground extinction, the SED from g' to K_S was fitted with a power law and dust reddening templates in the host at $z = 2.692$. Using extinction templates from the Milky Way (MW), Large (LMC) and Small Magellanic Cloud (SMC) and supernovae-induced dust (Pei 1992; Maiolino et al. 2004; Stratta et al. 2007), no signatures of dust extinction in the GRB host are evident down to 1σ confidence limits of $A_V^{\rm host} < 0.06$ mag (MW), $A_V^{\rm host} < 0.07$ mag (LMC), $A_V^{\rm host} < 0.05$ mag (SMC and SNe induced). Therefore, the effect of dust reddening is considered as negligible in the following analysis. The deviation from a power-law SED in the GROND g' band is consistent with Lyman-α absorption in the GRB host at $z = 2.692$.

3.2. The X-ray Afterglow Light Curve

In addition to the variable and densely sampled light curve in the GROND filter bands, the X-ray afterglow is bright and well covered by XRT observations. Similar to what is seen in the optical bands, the X-ray data show strong variability and the underlying afterglow is poorly constrained. After excluding the very early data, where there are no GROND observations ($t - T_0 < 300$ s), we fitted the remaining data using a similar procedure as used for the optical bands with a combination of smoothly connected power laws. Remarkably, the obtained late power-law index $\alpha_X = 0.99 \pm 0.12$ is compatible with the best fit from the GROND data $\alpha_o = 0.97 \pm 0.06$, providing additional evidence that the applied model fitting traces the underlying power-law decay of the afterglow reasonably well. The XRT light curve and the residuals to the power-law fits are shown in Figure 5. After flaring episodes, the XRT light curve drops back to the power law, consistent with the rebrightenings observed in previous GRBs or XRFs (e.g., Burrows et al. 2005a; Romano et al. 2006b). All XRT light curve data have been obtained from the *Swift* XRT light curve online repository (Evans et al. 2007).

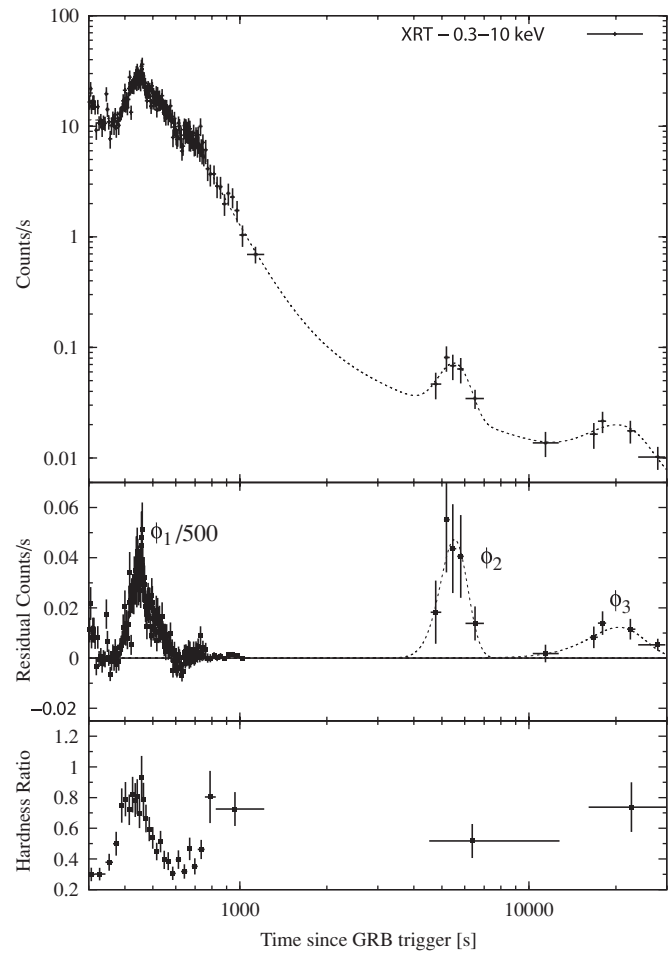

Figure 5. XRT light curve of the afterglow of XRF 071031 in the time domain simultaneous to the GROND data (top panel). The middle panel shows the residuals to the smoothly connected power-law fit, as well their modeling using Gaussians. The residuals of the first flare have been scaled by 1/500. The bottom panel shows the hardness ratio of the 1.5–10 vs. 0.3–1.5 keV band.

3.3. The Bumps

Both X-ray and optical/NIR data show significant variations from the typical power-law profiles at very early times. While this is observed in nearly 50% of all X-ray afterglows (e.g., Nousek et al. 2006), this is rarely seen so early in an optical light curve starting $\sim$400 s after the trigger.

We fitted the combined white light data with a canonical afterglow rise and decay with superimposed Gaussian profiles to account for the variations in the light curve. While this may not be the true physical model, it provides a good fit to the data and represents the morphology of the bumps with

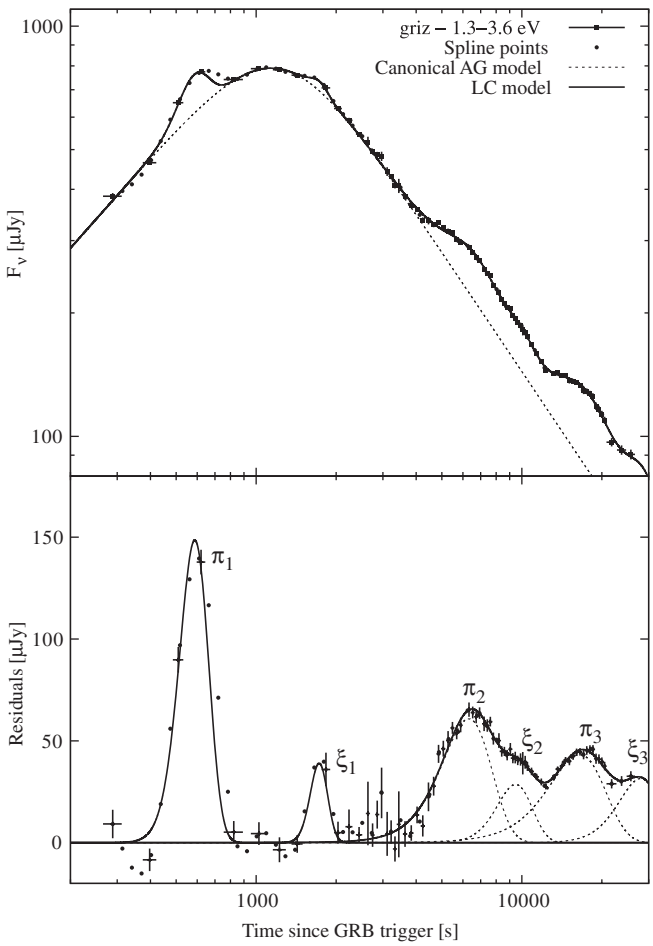

Figure 6. White light curve of the afterglow of XRF 071031 (upper panel, shown are the data and the cubic spline interpolation with equally spaced nodes in log(t)). The data were fitted using the sum of a smoothly connected power law for the canonical afterglow (dashed line) and Gaussian profiles to account for the evident flux excess (solid line). The lower panel shows the residuals to the smoothly connected power law, as well their modeling by six Gaussians.

adequate accuracy. For the very early optical data, where the time sampling of the light curve is naturally sparse, we used a cubic spline interpolation with equally spaced nodes in the native log–log scale of the afterglow to constrain the fit. The data suggest the existence of three major and three small bumps: the three brighter ones, π_1 to π_3, which peak at 0.6, 6, and 18 ks, and three fainter ones, ξ_1 to ξ_3, all shown in the lower panel of Figure 6. The first faint bump is only indicated by one data point and the last peak is not sampled by the observations due to the break of dawn. The fit shown in Figure 6 has a $\chi^2_{\rm red} = 1.05$ with 52 dof. The best-fit parameters are presented in Table 2.

The typical timescale of variation for the optical bumps is $\langle \Delta T/T \rangle = 0.35 \pm 0.13$, where ΔT is calculated as the full width at half maximum of the Gaussian, and they have a relative flux increase with respect to the underlying afterglow of $\langle \Delta F/F \rangle = 0.29 \pm 0.18$. All bumps, which are reasonably sampled by our observations, have a change in the slope $\delta\alpha$ between 0.5 and 0.9, which can be directly deduced from the lower panel of Figure 4.

Due to the faintness of the source, the late X-ray afterglow light curve is not as equally well sampled as the optical and a detailed analysis is not possible in late epochs. There is, however, evidence for three X-ray flares ϕ_1 to ϕ_3 between 350 and 25,000 s with synchronous optical coverage. To derive the morphology of the flares in the XRT light curve, we use a similar approach as for the optical bands for a direct comparison: an underlying continuum fitted with power laws and superimposed Gaussians to account for the evident flux excess which yields a reduced $\chi^2_{\rm red}$ of 1.15 for 154 dof. The best fit is shown in Figure 5 and the corresponding parameters are reported in Table 3.

The X-ray flares are much stronger $\langle \Delta F/F \rangle = 1.28 \pm 0.28$ with respect to the underlying afterglow than the optical bumps. Comparing against a statistical sample of previous X-ray flares (Chincarini et al. 2007) shows that the flares observed in XRF 071031 populate a similar phase-space region of $\Delta T/T$ versus $\Delta F/F$ and thus resemble the morphology of previous flares.

3.4. Spectral Evolution

The spectral index β, where $F_\nu \propto \nu^{-\beta}$, of the optical/NIR SED is observed to evolve with time (Figure 7). Remarkably, the chromatic evolution is correlated with the residuals of the data against the light curve fits. Applying a standard statistical correlation analysis yields a correlation coefficient of ~ -0.73, and thus a null hypothesis probability of $\sim 10^{-6}$.

The correlation of spectral hardening and bumpiness suggests that this is an intrinsic feature of the emission component in the bumps, rather than the afterglow itself. In the ISM model, for example, the cooling frequency ν_c moving through the optical bands would identify itself by a spectral softening (Sari et al. 1998), in contrast to the observations. A hardening of the spectrum would be expected in a windlike environment (Granot & Sari 2002) with a change in the spectral index of 0.5. The observed change (see Figure 7) is ~0.2 and therefore not compatible with a cooling break passing the optical bands also in the wind model.

In addition to the observed chromatic evolution in the optical bands, the X-ray data also show strong spectral changes throughout the observations. This is already indicated by the evolving hardness ratio of the two XRT bands (1.5–10 keV over 0.3–1.5 keV), shown in the lowest panel of Figure 5.

This evolution becomes more evident when individual early flares from Figure 1 are included in the analysis. For each flare in Table 4, a spectrum was extracted and fitted by single and broken power-law models. The rest-frame column density $N_{\rm H}$ at $z = 2.692$ was obtained by fitting the late photon counting

Table 2
Parameterization of the Excess Flux in the GROND Bands Using Gaussians

Bump	$T_{\rm mid}$ (s)	$\Delta T/2$ (s)	Amplitude (μJy)	$\Delta T/T_{\rm mid}$	$\Delta F/F$
π_1	587 ± 12	84 ± 18	149 ± 5	0.29 ± 0.06	0.24 ± 0.01
ξ_1	1726 ± 6	130 ± 4	39 ± 5	0.15 ± 0.01	0.06 ± 0.01
π_2	6302 ± 156	1648 ± 136	60 ± 5	0.52 ± 0.05	0.26 ± 0.02
ξ_2	9439 ± 377	1461 ± 254	29 ± 4	0.31 ± 0.06	0.18 ± 0.02
π_3	16505 ± 135	4013 ± 263	43 ± 2	0.49 ± 0.03	0.46 ± 0.02
ξ_3	28000	5000	32 ± 4	0.36	0.55 ± 0.03

Table 3
Parameterization of the Excess Flux in the X-ray Bands Using Gaussians

Bump	$T_{\rm mid}$ (s)	$\Delta T/2$ (s)	Amplitude (counts/s)	$\Delta T/T_{\rm mid}$	$\Delta F/F$
ϕ_1	459 ± 2	42 ± 2	14.5 ± 0.8	0.18 ± 0.01	1.36 ± 0.07
ϕ_2	5528 ± 85	604 ± 114	0.047 ± 0.01	0.22 ± 0.04	1.20 ± 0.20
ϕ_3	20507 ± 952	4557 ± 1088	0.012 ± 0.002	0.44 ± 0.10	1.28 ± 0.13

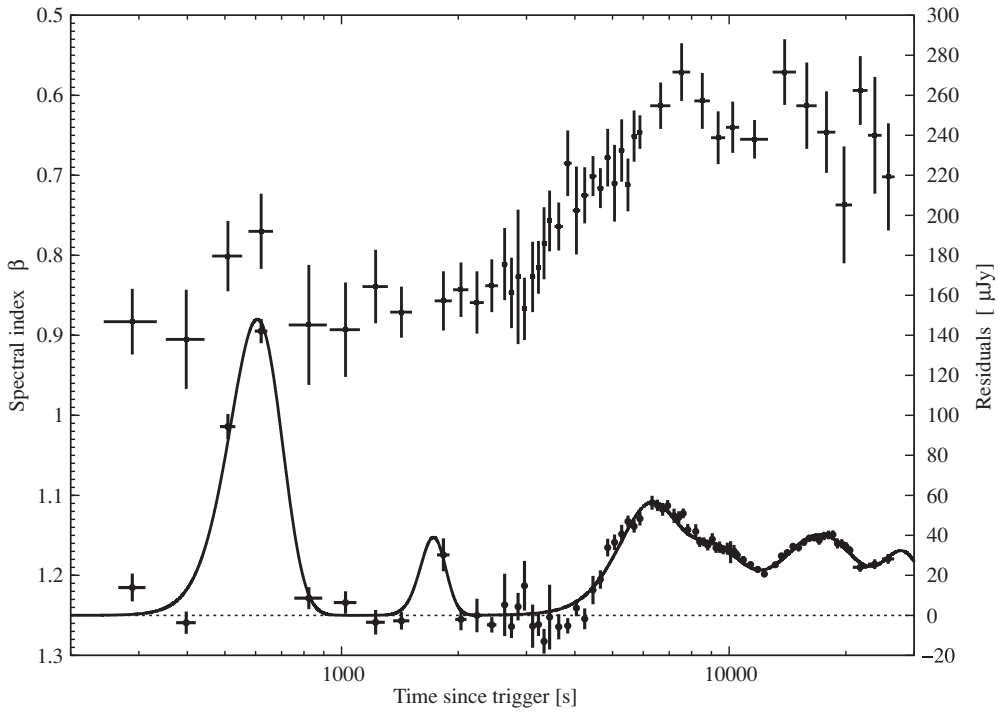

Figure 7. Color evolution of the optical/NIR afterglow of XRF 071031. A direct comparison of the spectral index β (upper points, left y-axis) against the residuals to a fit of a canonical afterglow light curve model (lower points, right y-axis). The plot clearly indicates a correlation of the spectral hardening and the rebrightening episodes in the light curve.

data and found to be consistent with zero within a 1σ confidence level. Combined with the negligible $A_{\rm V}$ from the optical data and assuming a constant $N_{\rm H}$ in the burst environment, the intrinsic $N_{\rm H}$ is neglected in the spectral fits. There is strong evidence that the flares are better modeled by broken rather than single power laws as shown in Table 4, which is similar to flares seen in, e.g., GRB 051117A (Goad et al. 2007), GRB 050713A (Guetta et al. 2007), and GRB 061121 (Page et al. 2007).

From the X-ray data alone, there is evidence for a break in the spectrum in the 1 keV range for the early flares. This is consistent with the result of Butler & Kocevski (2007), who find that the peak energy of the flare spectrum $E_{\rm P}$ crosses the X-ray bands on a typical timescale of 10^2 to 10^4 s. Combining the excess flux in the optical bands for π_1 and the X-ray spectrum in ϕ_1, the spectrum can be constrained over a broad energy range. For the optical bands the dominant emission process is FS emission even at early times, and the afterglow model fitting was used to disentangle the different components. In this way estimates of the flux attributed to the flare component can be obtained. As shown in Figure 8, the broadband spectrum of the first flare is reasonably well ($\chi^2 = 129$ with 114 dof) described by a Band function (Band et al. 1993) with an $E_{\rm P}$ of 1.79 ± 0.59 keV and a very reasonable set of parameters $\alpha = -0.78 \pm 0.03$ and $\beta = -1.92^{+0.11}_{-0.17}$ as compared to the BATSE sample (Kaneko et al. 2006).

We caution that this fit implicitly assumes that the excess emission seen in the optical bands is correlated with the X-ray flare and the applied model of the underlying FS emission traces the afterglow reasonably well. As the fundamental shape of the afterglow can be different than the empirical Beuermann profile, this might introduce significant systematic errors in the analysis. Additionally, an underestimated or even varying column density $N_{\rm H}$ would change the soft X-ray absorption and thus the overall broadband and X-ray fits.

For the later flares, the different components attributed to FS and flare emission cannot be deconvolved with high certainty. The X-ray data are faint and affected by the underlying afterglow, and the excess flux in the optical bands is strongly dependent on the parameters of the light curve fitting. In particular, there is a strong ambiguity between the sharpness of the break and the light curve decay. Given the large uncertainties, the optical color attributed to later bumps is compatible with the slope of the lower energy part of the Band function found for the first flare. $E_{\rm P}$, however, can no longer be constrained, but it is interesting to speculate that a similar Band function with an $E_{\rm P}$ between the optical and X-ray bands would account for the observed excess fluxes.

4. DISCUSSION

4.1. The Likely Cause of the Flares

Previously, bumps or flares in optical afterglow light curves have been reproduced using either a superimposed reverse shock component for early flares, inhomogeneities in the circumburst

Table 4
Spectral Fits to the X-Ray Flares Using XSPEC

Flare	Times (s)	Model	Photon index 1	Break energy (keV)	Photon index 2	χ^2/dof
1	137–150	Single	$1.23^{+0.05}_{-0.05}$	–	–	323/131
1	137–150	Double	$0.72^{+0.09}_{-0.09}$	$1.84^{+0.17}_{-0.36}$	$1.85^{+0.12}_{-0.19}$	157/129
2	189–217	Single	$1.72^{+0.09}_{-0.05}$	–	–	180/85
2	189–217	Double	$1.14^{+0.14}_{-0.15}$	$1.26^{+0.16}_{-0.13}$	$2.20^{+0.13}_{-0.11}$	89/83
3	236–284	Single	$1.87^{+0.05}_{-0.05}$	–	–	146/74
3	236–284	Double	$1.23^{+0.19}_{-0.18}$	$1.07^{+0.16}_{-0.12}$	$2.39^{+0.17}_{-0.14}$	67/72
4 (Φ_1)	396–547	Single	$1.64^{+0.04}_{-0.04}$	–	–	172/110
4 (Φ_1)	396–547	Double	$1.26^{+0.19}_{-0.32}$	$0.98^{+0.22}_{-0.20}$	$1.88^{+0.08}_{-0.08}$	120/108

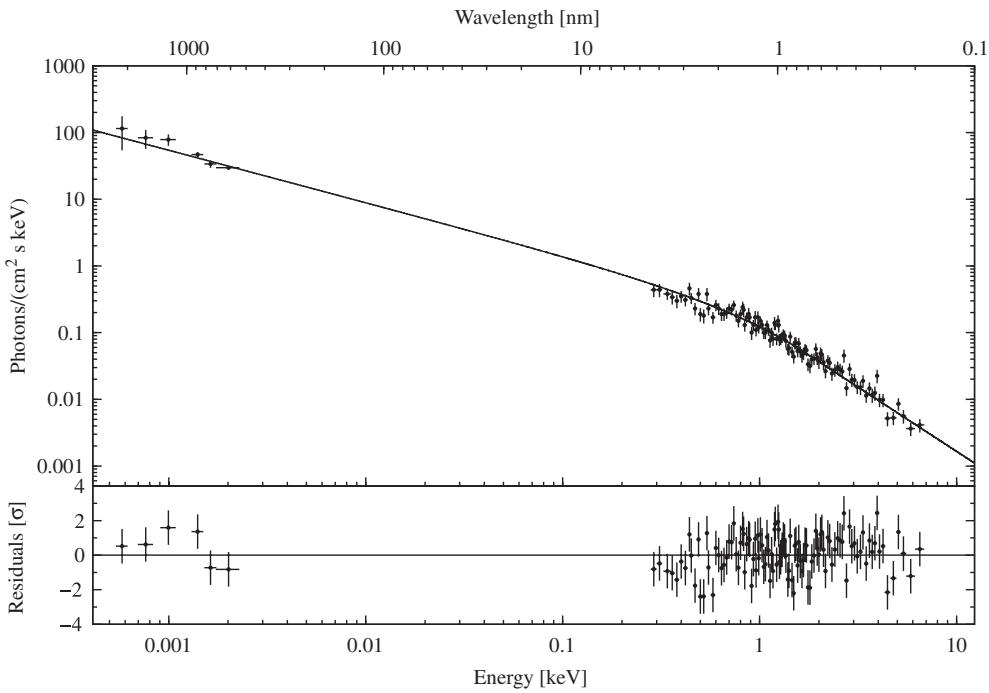

Figure 8. Broadband spectrum of the first flare π_1 with simultaneous optical and X-ray coverage. The data are fitted by a Band function with $E_P = 1.79 \pm 0.59$ keV, $\alpha = -0.78 \pm 0.03$, and $\beta = -1.92^{+0.11}_{-0.17}$.

medium (e.g., Wang & Loeb 2000), or the angular distribution of the energy in the jet (patchy shell model; e.g., Kumar & Piran 2000) or late energy injection by refreshed shocks (e.g., Rees & Meszaros 1998) for later flares. However, a clear discrimination in the individual previous cases was not possible due to the lack of simultaneous coverage in broad wavelength ranges.

Although we cannot completely rule out a reverse shock component for the first bump, it seems likely that it is produced by the same mechanism as the later ones. After subtracting the rising power law, the decline of the first bump can be fitted with a power law of index ~ -7. This would be surprisingly fast for a reverse shock, which is expected to decline with $\sim t^{-2}$ in the basic fireball model (e.g., Nakar & Piran 2004) and not faster than $\sim t^{-3}$ for more complicated models (Kobayashi 2000). The fact that the morphology is comparable to the later bumps additionally hints on a common origin. Therefore, we try to account for all bumps with as few assumptions as possible, thus searching for a phenomenological explanation for all bumps observed.

Recently, Nakar & Granot (2007) found that density jumps in the circumburst medium cannot account for the majority of fluctuations previously observed in GRB afterglow light curves. Only large contrasts in the circumburst medium density are able to produce bumps with a change in the temporal power-law decay index $\delta\alpha \approx 1$ in the light curve with a long transition time, which scales linearly with contrast. Thus, signatures of inhomogeneities in the circumburst medium in the optical light curve are expected to be smoother than what is observed.

A jet with inhomogeneities in the angular energy distribution produces episodic bumps when the cone of a relativistically beamed patch enters the field of view of the observer (Zhang et al. 2006). Similar to refreshed shocks, these patches inject additional energy into the blastwave, the afterglow emission is boosted to a higher level, and resumes the same power-law index as before the bump (Zhang & Mészáros 2002). A characteristic for rebrightenings due to patchy shells or refreshed shocks consequentially is a step-like afterglow light curve. Given the steepening of the power-law postbump (Figure 4), this scenario seems inconsistent with the bumps observed in XRF 071031. We note, however, that the refreshed shock scenario can produce rebrightenings on relatively short timescales under certain conditions, where the light curve drops back to the initial decay (e.g., Guidorzi et al. 2007).

Although the morphology of the light curve and optical bumps in the GROND data might be explained within the framework of variable external density or energy dissipation in the FS, both the

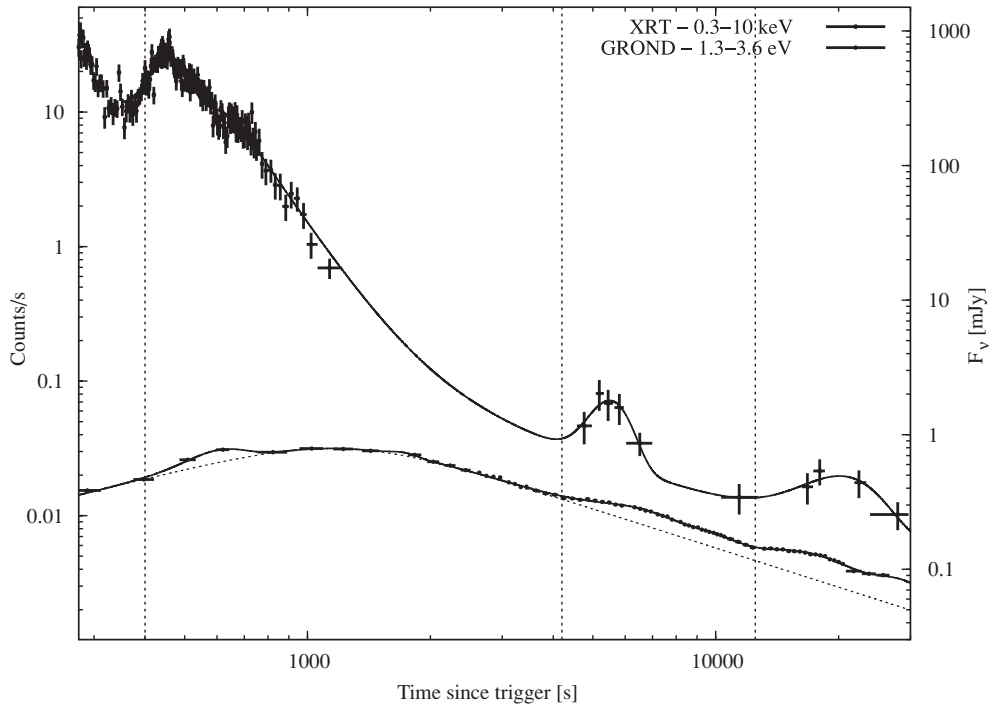

Figure 9. Combined plot of XRT light curve (crosses, left *y*-axis) and GROND white light (dots, right *y*-axis). The vertical dashed lines indicate the emergence of the bumps from the underlying optical afterglow emission.

spectral evolution and the correlation with the X-ray data argue for an independent origin and a second emission component. A hardening of the spectral index for flares in an optical light curve is not unprecedented (Greiner et al. 2009), and suggests a different emission than the generic afterglow FS. In addition, the first pronounced bump in the optical light curve is already observed during the rise of the afterglow at 600 s, when the apparent onset of the FS just started.

If all previously observed X-ray flares are due to the same physical process, it is very likely that they do not originate from external shocks that give rise to the afterglow emission, but from late time internal shocks (e.g., Burrows et al. 2005a; Zhang et al. 2006; Chincarini et al. 2007; Butler & Kocevski 2007). Thus, X-ray flares seem to be produced by a similar mechanism as the prompt γ-rays, which are also caused by internal shocks in the standard model (Rees & Meszaros 1992). Detailed analysis for GRB 050820A (Vestrand et al. 2006) showed that the optical emission contemporaneous with the prompt phase can be explained as the superposition of FS and emission correlated with the γ-rays. Similarly for XRF 071031, after subtracting the dominating FS in the optical bands, the flare spectrum from NIR to X-rays is well described with a Band function.

Remarkably, the optical bumps show features which have been previously observed in X-ray flares: a hardening of their spectra (e.g., Burrows et al. 2005a; Butler & Kocevski 2007; Falcone et al. 2007; Goad et al. 2007) and a correlation of the duration with the time where the bump occurs, i.e. a roughly constant $\Delta T/T$ (Chincarini et al. 2007; Kocevski et al. 2007). They are, however, less pronounced than typical X-ray flares. Temporal analysis of the early data shows that the optical bump peaks significantly later than the X-ray flare. A hard to soft evolution of $E_{\rm P}$ which is found in the majority of all bright flares where a detailed spectral analysis is possible (e.g., Burrows et al. 2005a; Romano et al. 2006a; Perri et al. 2007; Falcone et al. 2007) provides a natural explanation for the time difference between the flare in the X-ray and optical wavelength ranges. Spectral lags and a broadening towards lower energies have been observed in a number of previous X-ray flares and the prompt emission (e.g., Norris et al. 1996; Romano et al. 2006b; Perri et al. 2007).

Based on the light curve fitting, the observed peak of the early optical flare is delayed by $\tau \sim 130$ s compared to the X-rays, which corresponds to 35 s in the burst's rest frame. As the temporal coverage of the optical light curve is sparse in the early time frame, this delay is strongly dependent on the assumed functional form of the afterglow and flare morphology, but in any case it is significantly longer than what is typically observed as spectral lags in the prompt phase. Typical values for prompt lags range from slightly negative (i.e., soft preceding hard bands) to several seconds for long lag GRBs (e.g., Norris et al. 2000; Gehrels et al. 2006; McBreen et al. 2008; Foley et al. 2008). The observed time difference in the case of XRF 071031, however, is based on entirely different energy ranges. In particular, the difference between hard and soft energy bands is around a factor of 10^3 for X-rays versus optical, while it is $\sim$10 for BAT channels.

Combining bump morphology, color evolution, broadband spectrum, and the temporal connection to the X-ray data as shown in Figure 9, the most likely origin of the bumps in the optical/NIR light curve of XRF 071031 is the same as in the X-rays, namely the soft tail of emission correlated with late internal shocks.

4.2. Paucity of Detection of Correlated Early Optical Bumps and X-ray Flares

While a number of bursts have shown considerable variability in the optical bands during X-ray flares (e.g., Pandey et al. 2006; Boër et al. 2006; Page et al. 2007; Malesani et al. 2007), the early optical light curve is generally not as strongly affected as the X-rays by flaring episodes. The UVOT and ground-based robotic

telescopes with their fast response provide a good sample of optical observations simultaneous with the XRT light curve. If the first optical bump and the first X-ray flare in XRF 071031 are correlated as suggested by the data, the signature of a typical X-ray flare in the optical light curve can be approximated with the ratio of absolute optical to X-ray peak flux obtained for XRF 071031.

GRB 060607A, for example, showed significant X-ray flaring very early in the X-ray light curve with only marginally correlated optical emission (Ziaeepour et al. 2008). However, the afterglow was very bright, reaching ∼14.3 mag in the r band (Nysewander et al. 2009). If the flare was described with a similar spectrum as in XRF 071031, the expected optical counterpart of the brightest X-ray flare is estimated to have a peak amplitude of ∼200 μJy and could only be resolved with continuous photometric monitoring with a precision of at least 0.03 mag. Thus, if the emission in the flares is not strong enough with respect to the FS, a bright afterglow can easily outshine flare signatures in the optical bands even for very bright X-ray flares. In fact, GRB 061121 (Page et al. 2007) had simultaneous coverage with BAT, XRT, and UVOT of the prompt emission with a peak flux density in the X-rays of ∼15 mJy. Page et al. (2007) find that most of the flux is emitted in the γ-ray and X-ray bands, while the UVOT data showed only a relatively small increase in brightness.

5. CONCLUSIONS

The detailed light curve and spectral evolution of the afterglow of XRF 071031 showed several remarkable features. The most salient one is the achromatic early rise in brightness, resulting in a peak of the optical/NIR light curve at around 1 ks. The achromatic turnover from rise to decay suggests the apparent onset of the FS as its origin, due to either the increase in radiating electrons in the pre-deceleration phase or a structured outflow seen off-axis. In the latter case, the increase in brightness is caused by the deceleration of the shock, so that the relativistically beamed cone widens and gradually enters the sight line of the observer.

Superimposed onto the afterglow continuum emission are bumps which have a harder SED and appear in similar epochs in the optical/NIR as well as in the X-ray bands. Based on the GROND data collected for XRF 071031, we conclude that the variations in the light curve are most probably the optical counterparts of X-ray flares, and therefore directly connect variability in an optical light curve with the emergence of X-ray flares. Although emission from external shocks or a combination of different effects cannot be completely ruled out, an internal origin seems to nicely account for the majority of observations: the light curve shape and in particular the morphology of the bumps, the spectral hardening in the optical SED, the observed decrease in $E_{\rm P}$ from the prompt emission to the flares, and the broadband flare spectrum from NIR to X-rays. The spectral similarities to the prompt phase strengthen the picture of X-ray flares as later and softer examples of the prompt emission due to internal shocks. This connection provides additional evidence that inner engine activity may last or be revived on a timescale of hours or days at least for some bursts.

We thank the referee for a very helpful report and comments and D. H. Hartmann for discussion. This research was supported by the DFG cluster of excellence "Origin and Structure of the Universe." A.R. and S.K. acknowledge support by DFG grant Kl 766/11-3. Part of the funding for GROND (both hardware and personnel) was generously granted from the Leibniz Prize to Prof. G. Hasinger (DFG grant HA 1850/28-1). This work made use of data supplied by the UK *Swift* Science Data Centre at the University of Leicester.

REFERENCES

Adelman-McCarthy, J. K., et al. 2008, ApJS, 175, 297
Akerlof, C., et al. 1999, Nature, 398, 400
Arnaud, K. A. 1996, in ASP Conf. Ser. 101, Astronomical Data Analysis Software and Systems V, ed. G. H. Jacoby, J. Barnes (San Francisco, CA: ASP) 17
Band, D., et al. 1993, ApJ, 413, 281
Barthelmy, S. D., et al. 2005, Space Sci. Rev., 120, 143
Beuermann, K., et al. 1999, A&A, 352, L26
Blake, C. H., et al. 2005, Nature, 435, 181
Boër, M., Atteia, J. L., Damerdji, Y., Gendre, B., Klotz, A., & Stratta, G. 2006, ApJ, 638, L71
Breeveld, A. A., & Stroh, M. 2007, GRB Coordinates Network, 7028
Burrows, D. N., et al. 2005a, Science, 309, 1833
Burrows, D. N., et al. 2005b, Space Sci. Rev., 120, 165
Butler, N. R., & Kocevski, D. 2007, ApJ, 663, 407
Chincarini, G., et al. 2007, ApJ, 671, 1903
Cobb, B. E. 2007, GRB Coordinates Network, 7024
Covino, S., et al. 2008, MNRAS, 388, 347
Dai, Z. G., & Cheng, K. S. 2001, ApJ, 558, L109
de Ugarte Postigo, A., et al. 2005, A&A, 443, 841
Evans, P. A., et al. 2007, A&A, 469, 379
Falcone, A. D., et al. 2007, ApJ, 671, 1921
Foley, S., McGlynn, S., Hanlon, L., McBreen, S., & McBreen, B. 2008, A&A, 484, 143
Fox, A. J., Ledoux, C., Vreeswijk, P. M., Smette, A., & Jaunsen, A. O. 2008, A&A, 491, 189
Gehrels, N., et al. 2004, ApJ, 611, 1005
Gehrels, N., et al. 2006, Nature, 444, 1044
Goad, M. R., et al. 2007, A&A, 468, 103
Granot, J., & Sari, R. 2002, ApJ, 568, 820
Greiner, J., et al. 2007, The Messenger, 130, 12
Greiner, J., et al. 2008, PASP, 120, 405
Greiner, J., et al. 2009, ApJ, 693, 1912
Guetta, D., et al. 2007, A&A, 461, 95
Guidorzi, C., et al. 2005, ApJ, 630, L121
Guidorzi, C., et al. 2007, A&A, 474, 793
Haislip, J., et al. 2007, GRB Coordinates Network 7022
Kalberla, P. M. W., Burton, W. B., Hartmann, D., Arnal, E. M., Bajaja, E., Morras, R., & Pöppel, W. G. L. 2005, A&A, 440, 775
Kaneko, Y., Preece, R. D., Briggs, M. S., Paciesas, W. S., Meegan, C. A., & Band, D. L. 2006, ApJS, 166, 298
Kobayashi, S. 2000, ApJ, 545, 807
Kocevski, D., Butler, N., & Bloom, J. S. 2007, ApJ, 667, 1024
Krühler, T., Greiner, J., Afonso, P., Küpcü-Yoldaş, A., Yoldaş, A., & Szokoly, G. P. 2007, GRB Coordinates Network, 7021
Krühler, T., et al. 2008, ApJ, 685, 376
Kumar, P., & Piran, T. 2000, ApJ, 535, 152
Küpcü-Yoldaş, A., Krühler, T., Greiner, J., Yoldaş, A., Clemens, C., Szokoly, G., Primak, N., & Klose, S. 2008, in AIP Conf. Proc. 1000, Gamma-Ray Bursts 2007, ed. M. Galassi, D. Palmer, & E. Fenimore, 227
Lazzati, D., Rossi, E., Covino, S., Ghisellini, G., & Malesani, D. 2002, A&A, 396, L5
Ledoux, C., Jakobsson, P., Jaunsen, A. O., Thöne, C. C., Vreeswijk, P. M., Malesani, D., Fynbo, J. P. U., & Hjorth, J. 2007, GRB Coordinates Network, 7023
Lipkin, Y. M., et al. 2004, ApJ, 606, 381
Maiolino, R., Schneider, R., Oliva, E., Bianchi, S., Ferrara, A., Mannucci, F., Pedani, M., & Roca Sogorb, M. 2004, Nature, 431, 533
Malesani, D., et al. 2007, A&A, 473, 77
McBreen, S., Hanlon, L., McGlynn, S., McBreen, B., Foley, S., Preece, R., von Kienlin, A., & Williams, O. R. 2006, A&A, 455, 433
McBreen, S., et al. 2008, ApJ, 677, L85
McGlynn, S., et al. 2005, Nuovo Cimento C, 28, 481
Molinari, E., et al. 2007, A&A, 469, L13
Monet, D. G., et al. 2003, AJ, 125, 984
Nakar, E., & Granot, J. 2007, MNRAS, 380, 1744
Nakar, E., & Piran, T. 2004, MNRAS, 353, 647

Norris, J. P., Nemiroff, R. J., Bonnell, J. T., Scargle, J. D., Kouveliotou, C., Paciesas, W. S., Meegan, C. A., & Fishman, G. J. 1996, ApJ, 459, 393
Norris, J. P., Marani, G. F., & Bonnell, J. T. 2000, ApJ, 534, 248
Nousek, J. A., et al. 2006, ApJ, 642, 389
Nysewander, M., Reichart, D. E., Crain, J. A., Foster, A., Haislip, J., Ivarsen, K., Lacluyze, A., & Trotter, A. 2009, ApJ, 693, 1417
O'Brien, P. T., et al. 2006, ApJ, 647, 1213
Page, K. L., et al. 2007, ApJ, 663, 1125
Panaitescu, A., & Kumar, P. 2000, ApJ, 543, 66
Panaitescu, A., Meszaros, P., & Rees, M. J. 1998, ApJ, 503, 314
Panaitescu, A., & Vestrand, W. T. 2008, MNRAS, 387, 497
Pandey, S. B., et al. 2006, A&A, 460, 415
Pei, Y. C. 1992, ApJ, 395, 130
Perley, D. A., et al. 2008, ApJ, 672, 449
Perri, M., et al. 2007, A&A, 471, 83
Preece, R. D., Briggs, M. S., Mallozzi, R. S., Pendleton, G. N., Paciesas, W. S., & Band, D. L. 2000, ApJS, 126, 19
Racusin, J. L., et al. 2008, Nature, 455, 183
Rees, M. J., & Meszaros, P. 1992, MNRAS, 258, 41P
Rees, M. J., & Meszaros, P. 1998, ApJ, 496, L1
Romano, P., et al. 2006a, A&A, 456, 917
Romano, P., et al. 2006b, A&A, 450, 59
Roming, P. W. A., et al. 2005, Space Sci. Rev., 120, 95
Rykoff, E. S., et al. 2004, ApJ, 601, 1013
Sakamoto, T., et al. 2008, ApJ, 679, 570
Sari, R., & Piran, T. 1999, ApJ, 520, 641
Sari, R., Piran, T., & Narayan, R. 1998, ApJ, 497, L17
Schlegel, D. J., Finkbeiner, D. P., & Davis, M. 1998, ApJ, 500, 525
Skrutskie, M. F., et al. 2006, AJ, 131, 1163
Smith, J. A., et al. 2002, AJ, 123, 2121
Stamatikos, M., et al. 2007, GRB Coordinates Network 7029
Stratta, G., Maiolino, R., Fiore, F., & D'Elia, V. 2007, ApJ, 661, L9
Stroh, M. C., Falcone, A., & Racusin, J. L. 2007a, GRB Coordinates Network, 7027
Stroh, M. C., et al. 2007b, GRB Coordinates Network 7020
Tody, D. 1993, in ASP Conf. Ser. 52, Astronomical Data Analysis Software and Systems II, ed. R. J. Hanisch, R. J. V. Brissenden, & J. Barnes (San Francisco, CA), 173
Vestrand, W. T., et al. 2005, Nature, 435, 178
Vestrand, W. T., et al. 2006, Nature, 442, 172
Wang, X., & Loeb, A. 2000, ApJ, 535, 788
Zhang, B., Fan, Y. Z., Dyks, J., Kobayashi, S., Mészáros, P., Burrows, D. N., Nousek, J. A., & Gehrels, N. 2006, ApJ, 642, 354
Zhang, B., & Mészáros, P. 2002, ApJ, 566, 712
Zhang, B., & Mészáros, P. 2004, International Journal of Modern Physics A, 19, 2385
Ziaeepour, H., et al. 2008, MNRAS, 385, 453